

Barrier distributions from the fusion of oxygen ions with $^{144,148,154}\text{Sm}$ and ^{186}W

J. R. Leigh, M. Dasgupta, D. J. Hinde, J. C. Mein, C. R. Morton, R. C. Lemmon,* J. P. Lestone,† J. O. Newton, H. Timmers, and J. X. Wei‡

Department of Nuclear Physics, Research School of Physical Sciences and Engineering, Australian National University, Canberra, Australian Capital Territory 0200, Australia

N. Rowley§

Department of Astronomy and Physics, The University of Manchester, Manchester M13 9PL, United Kingdom and Department of Physics, University of Surrey, Guilford, GU2 5XH, United Kingdom

(Received 22 June 1995)

Fusion excitation functions for the reactions $^{144,148,154}\text{Sm}$ and $^{186}\text{W} + ^{16}\text{O}$ and $^{144}\text{Sm} + ^{17}\text{O}$ have been measured with high precision, both in the cross sections and the small energy intervals, thus allowing meaningful fusion barrier distributions to be extracted. In this representation it is clearly seen that the excitation functions are not smooth and featureless; each is unique and is shown to depend on the details of the structure of the interacting nuclei. The effects of excitation of the collective single phonon states in ^{144}Sm are evident. For the ^{17}O projectile, the role of additional coupling to neutron stripping channels with positive Q values can be seen. As expected, the barrier distributions associated with ^{154}Sm and ^{186}W are dominated by deformation effects. However, the data appear to display sensitivity to additional couplings, even though they involve relatively weak inelastic and transfer channels.

PACS number(s): 25.70.Jj

I. INTRODUCTION

Heavy-ion fusion cross sections at energies well above the Coulomb barrier can be reproduced by a barrier penetration model in which the one-dimensional fusion barrier results from a combination of the repulsive Coulomb and centrifugal potentials and the attractive, short range nuclear potential. At energies below this single barrier, measured fusion cross-sections σ_{fus} are generally enhanced relative to calculations with this model. The role of static deformation effects in enhancing sub-barrier fusion has long been recognized [1,2] and has been demonstrated experimentally [3,4]. Here the enhancement occurs because there is a distribution of barrier heights which can be thought of as resulting from different orientations of the deformed target nuclei. Any distribution of barriers around the single barrier leads to enhancement of the cross sections, at energies below that of the single barrier, because passage over the lower barriers is much more probable than penetration through the single barrier. The effects of collective surface vibrations on fusion were also considered [5] in a semiclassical picture, again resulting in a distribution of fusion barriers. The term "sub-barrier" fusion is conventionally used to describe fusion at energies below the single fusion barrier, even though the cross sections result largely from passage *over* barriers

whose heights are lower than the bombarding energy.

The subject of sub-barrier heavy ion fusion received further impetus following the observation [6,7] that the enhancement of the cross sections was a general phenomenon and not necessarily associated with the static or dynamic deformations of the reactants. This recognition inspired the idea that coupling between the relative motion and any nuclear degrees of freedom might be important. Theoretical investigations of coupling to inelastic [8] and transfer channels [9,10] were carried out in a coupled-channels framework and these again gave rise to a distribution of fusion barriers. In the case of nuclei with a static deformation, it was later demonstrated [11] that the classical picture is equivalent to the quantum mechanical coupled-channels approach, in the limit of zero energy for the rotational states, in that the two descriptions give rise to the same barrier distributions.

The importance of the distribution of fusion barriers was recognized in Refs. [2,12,13], where attempts were made to use fusion data to define some properties of the distribution. The major problem with these approaches was that the form and symmetry of the barrier distributions were built into the analyses. The first attempt to extract a barrier distribution directly from fusion data, using an unfolding procedure, was performed in Ref. [14]. The distributions were reasonably well defined at low energies but around the peak of the distribution, near the average barrier, the uncertainties were larger than the measured values. Only qualitative comparisons between the data and simple model calculations could be made and so this procedure has not been pursued.

It was recently shown analytically [15] that the distribution of barrier heights in a reaction could be extracted *directly* from a fusion excitation function using the second derivative of $E\sigma_{\text{fus}}$ as a function of energy E . The degree to which this relationship holds is illustrated in Fig. 1 by con-

*Present address: National Superconducting Cyclotron Laboratory, Michigan State University, East Lansing, Michigan 48824.

†Present address: Nuclear Physics Laboratory, University of Washington, Seattle, WA 98195.

‡Present address: Department of Astronomy and Physics, The University of Manchester, Manchester M13 9PL, United Kingdom.

§Permanent address: DRAL Daresbury Laboratory, Warrington, WA4 4AD, United Kingdom.

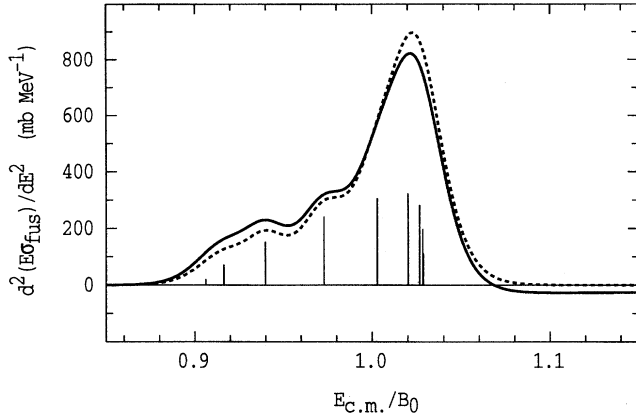


FIG. 1. Barrier distributions associated with a set of discrete barriers with weights represented by the height, and energies relative to the average value B_0 represented by the position of the vertical lines. The dashed line shows the smoothing effect of barrier penetration whilst the solid curve is the second differential of $E\sigma_{\text{fus}}$ from a realistic calculation; this is an excellent representation of the smoothed barrier distribution.

sidering a set of discrete barriers. The discrete barriers are shown by vertical lines whose positions are the barrier energies, relative to the average barrier B_0 , and whose lengths represent the probability of encountering that barrier.

In a classical sharp cutoff model,

$$E\sigma_{\text{fus}} = \pi R^2 \sum_{\alpha} w_{\alpha}(E - B_{\alpha}), \quad (1)$$

where R is the fusion radius, w_{α} is the barrier weight, and the B_{α} is the barrier energy associated with the channel index α . In this case, $d^2(E\sigma_{\text{fus}})/dE^2$ returns the original discrete barrier distribution as a set of delta functions, normalized by the w_{α} , at the barrier energies [15].

When quantum mechanical penetration of the barriers is considered, the cross sections vary smoothly in the vicinity of each barrier and $d^2(E\sigma_{\text{fus}})/dE^2$ becomes continuous. A calculation in which the radius and curvature $\hbar\omega$ of each barrier is assumed to be the same produces the distribution shown by the dashed line in Fig. 1, which is identical to the distribution obtained by smoothing the discrete distribution with a near Gaussian function [15] with a width of $0.56 \hbar\omega$.

The solid line in Fig. 1 shows the result of a more realistic calculation in which the dependence of the barrier radius and curvature on the angular momentum $l\hbar$ and the barrier energy is included. The reduction in the mean fusion radius with increasing energy, as a result of the increase in the mean l , is responsible for the negative values of $d^2(E\sigma_{\text{fus}})/dE^2$ at energies above the barrier region.

The differences between the two curves in Fig. 1 demonstrate the degree to which the second derivative of $E\sigma_{\text{fus}}$, represented by the solid line, differs from the smoothed barrier distribution, shown by the dashed line. Since the differences are small, it is convenient to refer to $d^2(E\sigma_{\text{fus}})/dE^2$ as the barrier distribution. Experimental data are measured at discrete energies and the barrier distribution is extracted us-

ing a point difference formula. For consistency, when comparing an experimental distribution with theory, we evaluate the theoretical distribution in an identical manner. We have made no attempts to unfold the effects of quantum mechanical barrier penetration in order to extract the true barrier distribution because in an exact coupled-channels approach for example, there are no explicit barriers for comparison.

Before the start of this work, fusion cross sections had typically been measured to an accuracy of $\approx 10\%$ at intervals between 2 MeV and 5 MeV. Such data yield poorly defined barrier distributions [15,16] and can therefore be equally well reproduced with models incorporating very different barrier distributions. Analyses of such data gave rise to a generally accepted belief that fusion excitation functions are smooth and featureless and do not provide a good test of models [17,18]. When the cross sections have high precision (typically $\approx \pm 1\%$) and are measured in small, precisely determined energy steps, the barrier distributions are well defined and they place more stringent limits on any models used.

In the past, the typical procedure which was followed in fitting an excitation function had been to fit the higher energy data using a calculation with a single barrier and then to successively introduce couplings (first to inelastic channels in the target, then in the projectile, and finally to transfer channels if necessary) until the calculated cross sections at the lowest energies matched the trend of the data. The success of the model calculation was then judged by its ability to fit these low energy data, which was often achieved at the expense of reproducing higher energy data less well. Possible dangers in this approach, and the advantages of being able to “see” the barrier distribution, are illustrated in Fig. 2 where three theoretical excitation functions for reactions involving different coupling schemes are shown. The coupling schemes involve coupling to a single channel with a negative Q value in Fig. 2(a), a positive Q value in Fig. 2(b), and coupling associated with a deformed nucleus in Fig. 2(c).

The three calculated excitation functions are essentially identical at the highest and lowest energies and fitting these regions with a model does not necessarily mean that the correct couplings have been incorporated. In this example, the excitation functions differ significantly in the range of $E_{\text{c.m.}}/B_0$ between 0.97 and 1.05 MeV where differences of up to a factor 2 occur. Even with these large differences, the type of coupling involved is not immediately apparent from the excitation functions themselves. It is possible to use theoretical guidance in assessing the *likely* couplings in a particular reaction and subsequent fitting of the cross sections may be used to interpret the excitation function. In contrast, the shapes of the barrier distributions, shown in the lower half of the figure, are more easily interpreted and reveal directly where the barrier strength lies, without recourse to detailed theoretical calculations.

The calculations in Fig. 2 were performed for a specific reaction but details of the calculation are unimportant since the conclusions are expected to apply generally; cross sections for any reaction at energies well above and well below the barrier from one calculation can be reproduced by the others if the Q values, coupling strengths, and deformations are treated as free parameters.

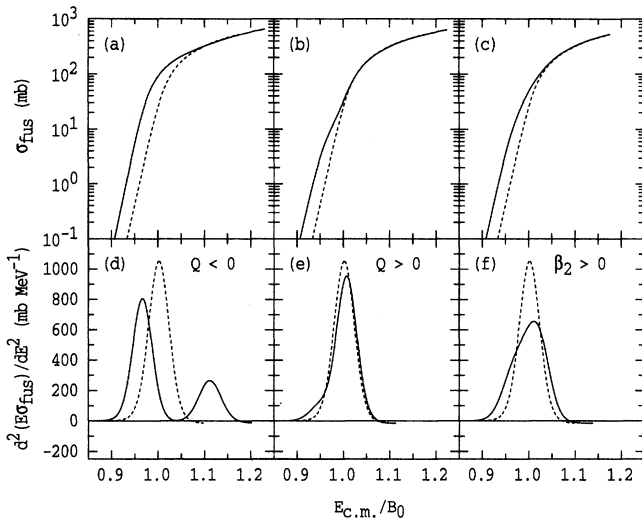


FIG. 2. Calculated excitation functions and barrier distributions for a single barrier (dotted lines) compared with three coupling schemes involving coupling to a negative Q value channel (a) and (d), a positive Q value channel (b) and (e), and coupling associated with a nucleus with a permanent quadrupole deformation (c) and (f). The excitation functions, plotted as the ratio of the energy to the average barrier B_0 , are essentially identical at low and high energies. The type of coupling is more easily seen in the lower part of the figure than in the excitation functions themselves.

We do not wish to imply that the barrier distributions contain more information than the excitation functions from which they are derived; clearly this cannot be so. There are, however, several advantages to this form of representation, not the least of which is that the fine structure in an excitation function becomes more apparent. The barrier distributions can also be used to indicate whether data are of sufficient quality to serve as a useful test of models, since if the barrier distribution is not well defined the data are too imprecise. Finally, as illustrated in the lower half of Fig. 2, a barrier distribution gives a strong indication of the important channel couplings. It should be noted that the interpretation of an experimental barrier distribution is not always as simple as suggested by the examples shown in Fig. 2. These are idealized cases and in reality several different types of coupling may be involved in a given reaction, complicating the situation. Nonetheless, the ability to see directly how barrier strength is distributed can be useful in probing such questions as the following: are the theoretical coupling strengths associated with inelastic and transfer channels appropriate?; do the coupling strengths depend on the reaction Q value?; are there channels other than the obvious ones which play a significant role in fusion?; how well do the available models work?

This paper presents the excitation functions for five reactions, $^{144,148,154}\text{Sm} + ^{16}\text{O}$, $^{144}\text{Sm} + ^{17}\text{O}$, and $^{186}\text{W} + ^{16}\text{O}$, measured in small energy intervals and with high precision. Various aspects of the work have already been presented in condensed form [16,19–22]. These reactions were chosen to test the efficacy of the barrier distribution technique and to investigate specific coupling schemes. Based on earlier studies [23], the $^{144}\text{Sm} + ^{16}\text{O}$ reaction was expected to show a

distribution consistent with a single barrier, though some small effects could have been expected from couplings to the weak inelastic channels associated with the semimagic ^{144}Sm . The measurement with the ^{17}O projectile was chosen to study the additional effects of the neutron transfer channel. The use of the deformed ^{154}Sm and ^{186}W nuclei was intended to serve as an experimental test of the barrier distribution concept since the effects of deformation are well established and the barrier distributions are expected to be close to the classical ones, which are readily calculable. The ^{148}Sm nucleus lies between the spherical and statically deformed limits.

II. EXPERIMENTAL METHODS

The ANU 14UD Pelletron accelerator was used to provide beams of oxygen ions in the energy range 50–110 MeV. The beams were bunched to provide bursts of 1 ns full width at half maximum, separated by 533 ns. The samarium targets were typically $40 \mu\text{g}/\text{cm}^2$ in thickness and were produced by evaporating isotopically enriched metals onto self-supporting carbon foils of $\approx 20 \mu\text{g}/\text{cm}^2$. In the case of ^{186}W , enriched oxide material was sputtered onto the backing foil using a saddle-field ion source. For all targets, the carbon foils were masked to produce deposits in the form of a strip of width 2 mm. The targets were mounted with the target strip vertical in order to limit angular variation due to possible beam spot movement.

Evaporation residue (ER) differential cross sections were measured over an angular range from -5° to 10° using a position sensitive multiwire proportional counter (MWPC) located behind a compact velocity filter [24]. The apparatus was mounted on a moveable arm, housed in a 2 m diameter scattering chamber. The filter removed the intense elastically scattered beam particles whilst transmitting ER's with 100% efficiency. The geometrical efficiency of the MWPC was 98%, the 2% loss being due to the wires which were used for position determination. The efficiency of the combined filter and detector was measured by placing a silicon surface barrier (SSB) detector behind the entrance collimator and directly observing ER's at 8° where the elastic scattering was not too intense. The SSB detector was then removed and the ER yield was measured in the MWPC. The ratio of the latter to former was 1.03 ± 0.04 , indicating an efficiency for transmission and detection of the residues close to the expected value of 98%. We use the expected geometrical efficiency in evaluating cross sections. Details of the performance of the filter and the geometrical arrangement are given in Ref. [24]. The ER's were identified by their energy loss ΔE , position, and time of flight (TOF) relative to the pulsed beam; a spectrum of ΔE plotted against TOF is shown in Fig. 3.

At larger angles, ER's were also detected and identified by their energy and time of flight using a SSB detector with a solid angle about ten times that of the filter. It was mounted on the same moveable arm as the velocity filter but displaced from it by a nominal angle of 20° . This allowed direct observation of ER's at angles $> 10^\circ$, where the elastic rates were not excessive. All the ER yields were normalized to the Rutherford scattering yields in two SSB detectors, located at $\pm 30^\circ$.

The moveable arm on which the ER detectors are

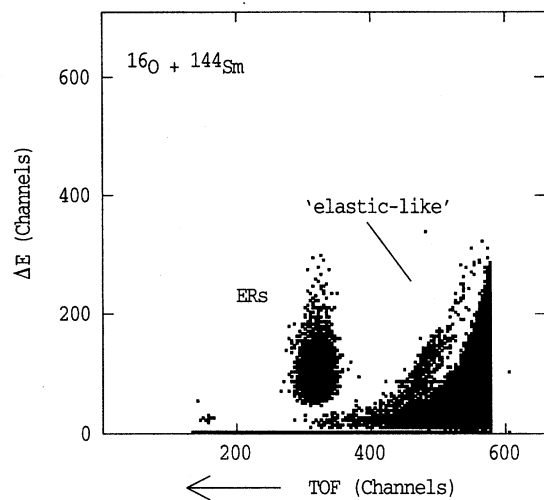


FIG. 3. Energy loss plotted against time of flight for $^{144}\text{Sm} + ^{16}\text{O}$ at 68 MeV. The ER's are well separated from the elasticlike events. There are 5000 events in the ER labeled group.

mounted is connected to an angle encoder with a readout that specifies the angle to only 0.1° . However, by always approaching the required angle from the same direction, it was determined that the angle could be consistently reproduced with an accuracy better than 0.01° . The absolute angles of the ER detectors were determined by the measurement of the ratio of the Rutherford cross sections at two angles with a well defined angular separation. Since the efficiency for transmission of elastically scattered particles through the velocity filter is small, and unknown, a SSB detector was introduced behind the defining aperture of the velocity filter for this calibration. Then, for nominal angles of $+10^\circ$ and -10° , separated by a well defined 20° , the true angles can be determined to $\leq 0.01^\circ$ if the relative cross sections are measured to $\leq \pm 0.5\%$. The calibration measurements were made at several pairs of angles, for instance $\pm 8^\circ$, $\pm 10^\circ$, $\pm 12^\circ$, and consistency between these measurements gave assurance that the target position was on the axis of rotation. Having established the absolute angles of the detectors, the measurement of elastic yields in the ER detectors, for known Rutherford differential cross sections, provides a calibration through which all ER yields can be converted into differential cross sections.

The beam energies were defined by the field in the analyzing magnet, measured with an NMR probe. A method of recycling the magnet [25] was consistently used to ensure differential hysteresis effects were minimized. Over a period of fifteen years the magnet constant has been measured on more than twenty occasions, after recycling the magnet, giving a standard deviation of 0.04%. The latest calibration measurement was performed during the course of this work using the $^{12}\text{C}(p, \alpha)^9\text{Be}$ resonance at 14.23 MeV and gave a magnet constant which was consistent with previous values. Thus for the fusion measurements, the absolute beam energy is defined to about ± 50 keV but relative energies have a much smaller uncertainty, as discussed below. The energy reproducibility has been checked frequently by remeasuring points in the excitation function after recycling the magnet;

the differential cross sections at 2° generally agree within the statistical errors of $\leq \pm 1\%$.

Excitation functions were obtained by measuring differential cross sections $d\sigma_{\text{fus}}(\pm 2^\circ)/d\Omega$ for ER's at $\pm 2^\circ$ at small energy intervals, typically 0.5 MeV. Full angular distributions were measured at intervals of 5 or 10 MeV. Typically, a series of measurements was made with monotonically increasing energies, for which the analyzing magnet was steadily increased, care being taken not to overshoot the desired field. The magnet was then recycled and a second excitation function was measured, at intermediate energies. For some reactions, as many as four independent sweeps were made. Selected points from the excitation functions were subsequently remeasured following magnet recycling. During the monotonic increase in field the energy intervals were defined to better than a few keV.

The differential cross section at $\pm 2^\circ$ for $^{154}\text{Sm} + ^{16}\text{O}$ at 90 MeV has now been measured nine times, in a series of different runs, giving a standard deviation of 0.3%, consistent with the statistical errors. This demonstrates that the potential difficulties associated with defining the beam energy and setting detector angles can be overcome such that their contribution to the uncertainty in the cross sections can be significantly smaller than $\pm 1\%$.

However, in the early experiments with the ^{154}Sm , ^{186}W , and ^{148}Sm targets, we found occasional cross sections which deviated considerably, by up to 7%, from those expected from interpolation of the neighboring points. Such scatter most probably arose from human error in following the intricate procedures in setting beam energies and detector angles. The point with the largest deviation was easily identified and rejected [16]. However, where the deviation is not so large, $\leq 4\%$, the points must be retained. Some scatter, greater than that expected statistically, is evident in the highest energy regions for these reactions and is particularly obvious in the barrier distribution representations. It is likely that this scatter arises from the poor application of the methods used, rather than the methods themselves.

The experimental procedures have been developed and refined, and with increasing experience, the data for the two reactions with the ^{144}Sm target were apparently free of such anomalies; here the cross sections generally had a scatter which was consistent with that expected statistically. For this reason, it was considered worthwhile to obtain data of higher statistical precision for these reactions in order to enable barrier distributions to be extracted which are better defined at the higher energies.

III. RESULTS

A. Cross sections

Typical ER angular distributions are shown in Fig. 4. Total ER cross sections were obtained by fitting these distributions using two Gaussian functions, indicated in Fig. 4, and analytically determining the areas under those Gaussians. This parameterization may be physically justified in a qualitative way by associating the wider Gaussian with emission of α particles from the recoiling composite system whereas the narrower one results from neutron and proton evaporation. Generally there were systematic differences in the shapes of the data and the fitted functions, which gave rise to

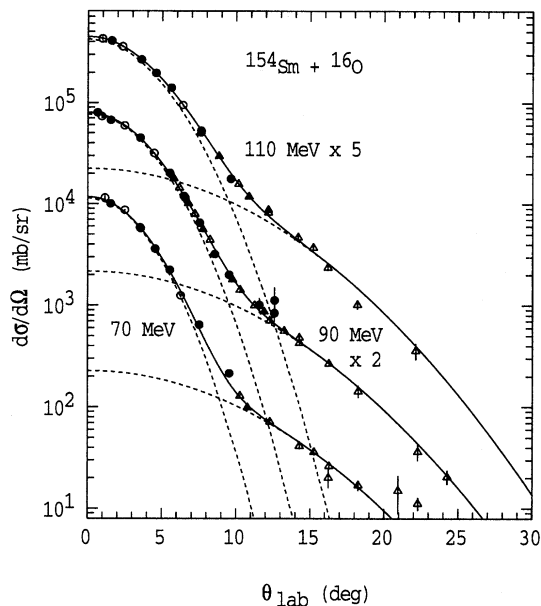


FIG. 4. Typical angular distributions of evaporation residues. The dashed lines are the two Gaussian functions used to obtain the total cross section at each energy. The filled and open circles are measurements using the velocity filter on opposite sides of the beam axis. The triangles are measured directly with a SSB detector.

values of χ^2 per degree of freedom χ^2_ν of typically between 2 and 4, when the statistical errors on the data points were typically $\approx \pm 1\%$, although larger errors apply when the yields are very low at large angles. However, the reliability of the extracted cross sections was confirmed by fitting, in an identical way, angular distributions calculated for a known cross section using the statistical model code PACE2 [26]. Since the targets are thin, multiple scattering of the ER's is negligible and the shapes of the angular distributions are determined by kinematics. Thus they are readily calculable if the multiplicity, energy, and type of the emitted particles are known. The statistical model calculations of the angular distributions should be a useful guide to their shapes. The fits to the PACE2 calculations showed similar systematic deviations and χ^2_ν values to those obtained in fitting the measured data. The fits, on average, underestimated the input cross sections by 0.2% and had a further scatter around the mean of about 0.3%. The small systematic shift may be expected to apply to the experimental data but has not been taken into account in the extracted cross sections.

Small movements in the beam spot position were determined from the relative yields in the two monitor detectors, allowing corrections of the differential cross sections at $\pm 2^\circ$ to be made.

Total ER cross sections were obtained from the differential values by interpolation using the measured ratios of $\sigma_{\text{fus}}/[d\sigma(2^\circ)/d\Omega]$. It should be noted that the measurements of the total cross sections need not be performed as part of the excitation function involving measurements of the differential cross sections. Indeed a totally different technique for measuring the total cross sections could be used. The total cross sections basically provide a series of points at

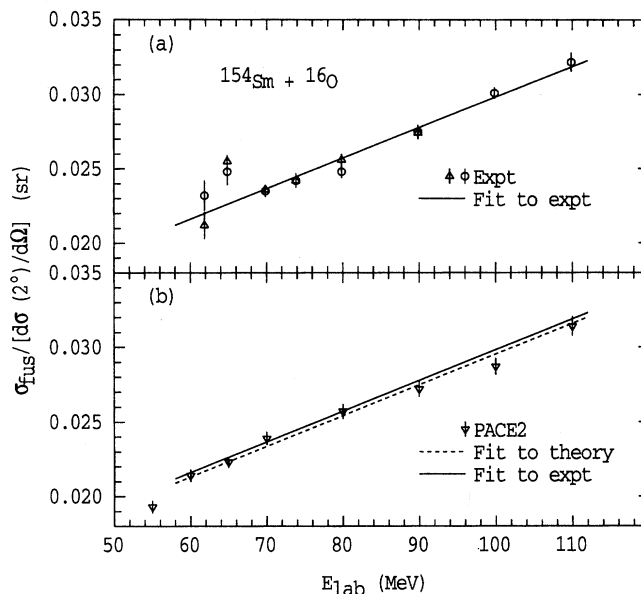


FIG. 5. (a) Experimental ratios of the total ER cross sections to the differential values at 2° for $^{154}\text{Sm} + ^{16}\text{O}$. The circles are obtained from the full angular distributions whereas the triangles use the same total cross sections but independent measurements of the differential values. (b) Calculated ratios using PACE2 (inverted triangles). The best fit to the experimental data is shown by the solid lines in (a) and (b). The fit to the PACE2 calculations is shown as a dashed line in (b). The lines have the same gradient but the calculation gives slightly smaller ratios than the data.

which the differential excitation function can be normalized. Two sets of data for $\sigma_{\text{fus}}/[d\sigma(2^\circ)/d\Omega]$ are presented in Fig. 5(a) for the reaction $^{154}\text{Sm} + ^{16}\text{O}$; one consists of the ratios obtained from the full angular distributions whilst the other is obtained from the same total cross sections and independent measurements of the differential values. The good agreement between the two sets is expected since the experimental conditions were the same for all measurements. The variation with energy is seen to be smooth and slow and a linear fit, also shown in the figure, is an excellent representation of the data. Statistically, there is an error of about $\pm 7\%$ in the gradient of the fitted line and this gives an error in the ratio of $\pm 0.5\%$ at the highest energies and $\pm 0.8\%$ at the lowest energies. Thus the interpolation is not expected to introduce significant errors. At beam energies below 70 MeV the experimental data scatter due to the difficulties in defining the shapes of the angular distributions because the yields at large angles are very small for these small cross sections. The low energy region is just that where the barrier distributions are well defined and larger errors on the cross sections would not significantly change the barrier distributions. Also, any deviation from the linear behavior would be gradual, giving small systematic errors in the cross sections. Arguments presented later show that such systematic errors do not affect our conclusions regarding the effectiveness of barrier distribution measurements.

The use of a linear function over the full energy region is supported by PACE2 calculations, as shown in Fig. 5(b).

TABLE I. Fusion cross sections for the indicated reactions. The errors quoted are statistical. The energies at which full angular distributions were performed are marked with an asterisk.

E_{lab} (MeV)	σ_{fus} (mb)	$\delta\sigma_{\text{fus}}$ (mb)	E_{lab} (MeV)	σ_{fus} (mb)	$\delta\sigma_{\text{fus}}$ (mb)
	$^{144}\text{Sm} + ^{16}\text{O}$		*89.88	852	4
62.88	0.15	0.08	*99.88	1072	7
63.38	0.33	0.08		$^{154}\text{Sm} + ^{16}\text{O}$	
63.88	0.45	0.08	57.86	0.18	0.05
64.38	1.5	0.2	58.36	0.19	0.04
64.88	2.7	0.3	58.86	0.81	0.06
65.38	5.5	0.3	59.36	1.06	0.09
65.88	10.2	0.4	59.86	2.4	0.2
66.38	17.5	0.3	60.36	3.6	0.3
66.88	28.6	0.3	60.86	5.1	0.3
67.38	41.3	0.4	61.36	7.7	0.3
*67.88	55.5	0.4	*61.86	11.0	0.4
68.38	71.2	0.5	62.36	15.4	0.5
68.88	90.6	0.6	62.86	19.4	0.4
69.38	108	1	63.36	25.2	0.4
*69.88	131	1	63.86	31.9	0.4
70.38	150	1	64.36	39.8	0.5
70.88	169	1	*64.86	46.8	1.2
71.38	184	1	65.36	61.5	0.7
71.88	208	1	65.86	74.3	0.8
72.88	253	2	66.36	87.1	1.0
73.88	295	2	66.86	103	1
*74.88	348	2	67.36	118	1
75.88	383	2	67.86	138	1
77.88	469	3	68.36	165	2
*79.88	552	3	68.86	186	2
*84.88	700	5	69.36	201	2
89.88	876	4	*69.86	222	2
*99.88	1076	15	70.36	247	4
	$^{144}\text{Sm} + ^{17}\text{O}$		70.72	263	3
60.88	0.07	0.05	71.36	295	3
61.38	0.11	0.07	71.86	318	3
61.88	0.19	0.09	72.36	341	4
62.38	0.40	0.09	72.86	354	4
62.88	0.81	0.23	73.36	375	4
63.38	1.2	0.2	*73.86	391	4
63.88	2.4	0.2	75.86	463	5
64.88	5.7	0.3	77.86	555	6
65.88	13.9	0.5	*79.86	630	6
66.88	30.8	0.6	*89.86	933	9
67.88	57.2	0.7	*99.86	1025	10
*68.88	90.5	0.9	*109.86	1229	13
70.01	137	1		$^{186}\text{W} + ^{16}\text{O}$	
70.88	171	1	67.86	0.35	0.08
71.88	209	1	68.36	0.40	0.09
72.88	253	2	68.86	0.9	0.2
73.88	296	2	69.36	1.0	0.1
74.88	345	2	69.86	1.7	0.2
75.88	383	2	70.36	2.9	0.2
76.88	428	2	70.86	4.5	0.3
77.88	463	3	*71.36	8.0	0.3
78.88	508	3	71.86	12.0	0.4
*79.88	548	3	72.36	17.9	0.5

TABLE I. (Continued).

E_{lab} (MeV)	σ_{fus} (mb)	$\delta\sigma_{\text{fus}}$ (mb)	E_{lab} (MeV)	σ_{fus} (mb)	$\delta\sigma_{\text{fus}}$ (mb)
72.86	24.9	0.4		¹⁴⁸ Sm+ ¹⁶ O	
73.36	33.4	0.4	60.86	0.4	0.1
*73.86	43.9	0.7	61.36	1.1	0.2
74.36	55.1	0.5	61.86	1.7	0.2
74.86	67.2	0.7	62.86	5.8	0.2
75.36	81.0	0.8	63.36	7.9	0.4
75.86	95.6	0.9	63.91	12.6	0.3
76.36	111	1	*64.86	25.0	0.4
76.86	130	1	65.36	31.0	0.7
77.36	149	2	65.86	43.4	0.4
77.86	165	2	66.86	70.7	0.7
78.36	183	2	67.40	83.0	0.8
78.86	214	2	67.86	105	1
79.36	222	2	68.86	145	2
*79.86	244	3	69.36	140	2
80.36	267	3	*69.86	179	2
80.86	285	3	70.86	233	3
81.36	310	3	71.36	260	3
81.86	323	3	71.86	274	3
82.36	340	3	72.86	318	4
82.86	373	4	73.86	356	4
83.86	405	6	*74.86	399	4
84.86	445	5	75.86	442	4
85.86	490	5	77.86	536	5
*89.86	626	6	*79.86	605	6
*99.86	918	9	81.86	652	7

Although there are small differences in the magnitude of the measured and calculated ratios, largely because the calculations underestimate the α -multiplicity, the energy dependence is well reproduced, as indicated by the lines in Fig. 5.

The measured fusion excitation functions are presented in Table I and in Fig. 6; the associated errors are statistical, though for the ¹⁸⁶W and ¹⁴⁴Sm reactions they have been modified by the following considerations.

In the case of the ¹⁸⁶W + ¹⁶O reaction, the most fissile system studied, the fusion cross section is the sum of the ER and fission components. The fission cross sections were taken from Ref. [27] and the uncertainties in fission cross sections are included in the errors quoted in the table. The individual ER and fission cross sections have been published in Ref. [21].

The ¹⁴⁴Sm target was enriched to 96.5% , with contamination of $\leq 1\%$ from each of the heavier Sm isotopes. A correction to the measured ER cross sections should be made to account for the contributions from these isotopes, particularly at the lowest energies where the cross sections associated with the highly deformed, heavier isotopes can be significant. This was achieved by using the measured cross sections presented here for ¹⁴⁸Sm and ¹⁵⁴Sm and those of Refs. [3,28] for the other isotopes. Interpolation to the required energies was performed using calculations which reproduced these data. In the calculations, the Sm nuclei were assumed to be statically deformed with the deformation parameters changing smoothly and systematically with mass. In the case of the ¹⁷O reaction, there are no data available.

Here, the corrections applied to the ¹⁶O data were scaled by the ratio of the cross sections calculated for the two projectiles incident on ¹⁴⁸Sm, where the ¹⁷O calculation included a positive Q value neutron stripping channel with a coupling strength taken from the fits to the ¹⁴⁴Sm + ¹⁷O excitation function, as discussed later. The errors have been increased to account for uncertainties in making these corrections.

The methods used to establish the absolute beam energy and to determine the detector angles, discussed in Sec. II, serve to minimize the associated *systematic* errors as well as the random errors. Additional systematic errors may result, for instance, from the conversion from differential to total cross sections and from the efficiency of the detector system. The errors associated with these identified sources are expected to be smaller than 1%.

B. Fusion barrier distributions

The second derivative of $E\sigma_{\text{fus}}$ was extracted from the excitation functions using a simple point difference method. It is defined at energy $(E_1 + 2E_2 + E_3)/4$ as

$$\frac{d^2(E\sigma_{\text{fus}})}{dE^2} = 2 \left(\frac{(E\sigma_{\text{fus}})_3 - (E\sigma_{\text{fus}})_2}{E_3 - E_2} - \frac{(E\sigma_{\text{fus}})_2 - (E\sigma_{\text{fus}})_1}{E_2 - E_1} \right) \left(\frac{1}{E_3 - E_1} \right), \quad (2)$$

where $(E\sigma_{\text{fus}})_i$ are evaluated at energies E_i .

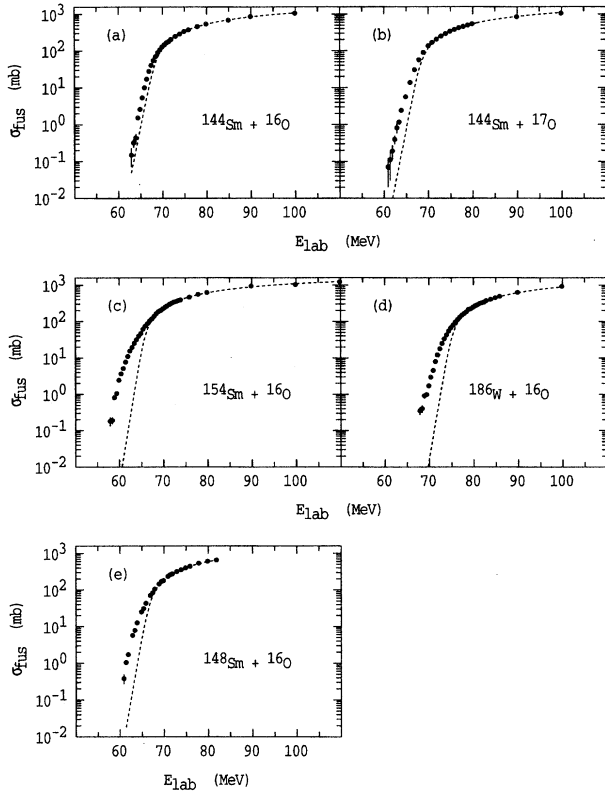


FIG. 6. Measured excitation functions for the indicated reactions. The dashed curves are calculated using the single barrier which best reproduces those cross sections above 200 mb.

With equal energy increments $\Delta E = (E_2 - E_1) = (E_3 - E_2)$ this reduces to

$$\frac{d^2(E\sigma_{\text{fus}})}{dE^2} = \left(\frac{(E\sigma_{\text{fus}})_3 - 2(E\sigma_{\text{fus}})_2 + (E\sigma_{\text{fus}})_1}{\Delta E^2} \right). \quad (3)$$

Then the statistical error δ_c associated with the second derivative at energy E is approximately given by

$$\delta_c \approx \left(\frac{E}{\Delta E^2} \right) [(\delta\sigma_{\text{fus}})_1^2 + 4(\delta\sigma_{\text{fus}})_2^2 + (\delta\sigma_{\text{fus}})_3^2]^{1/2}, \quad (4)$$

where the $(\delta\sigma_{\text{fus}})_i$ are the errors in the cross sections. They have dimensions of cross sections and are *not* percentage errors. Thus when, as is common, the σ_{fus} are measured with a fixed *percentage* error, δ_c is proportional to the value of σ_{fus} and increases with increasing energy. Hence δ_c would be an order of magnitude larger when $\sigma_{\text{fus}} = 1000$ mb than when $\sigma = 100$ mb. The barrier distribution is therefore well defined at the lowest energies where the cross sections are small, even though the percentage errors may be relatively large, but it becomes increasingly poorly defined as the energy increases. Generally, the measurements presented here have statistical errors $\lesssim \pm 1$ mb for σ_{fus} below 100 mb and $\lesssim \pm 1\%$ for larger cross sections.

The value of δ_c is also inversely proportional to ΔE^2 and can therefore be reduced if larger energy intervals are used.

Of course, large intervals smooth the extracted distribution, resulting in the damping of features in the distribution whose energy scale is smaller than the step length. Since the barrier distribution is already smoothed because of barrier penetration by $0.56\hbar\omega$, which is typically ≈ 2 MeV, using $\Delta E \approx 2$ MeV does not result in significant additional smoothing. A step length equivalent to 2 MeV in the laboratory frame has been adopted for all results presented here.

The fusion barrier distributions for the reactions studied are plotted in Fig. 7. An advantage of making measurements with intervals smaller than the step length used in the point difference method is that several barrier distributions can be generated, as shown in Ref. [16], and their consistency increases confidence in the shape of the distributions. It is apparent that the barrier distribution is an extremely sensitive method of displaying an excitation function. The shapes of the distributions in Fig. 7 are all different and show features which are not evident in the conventional representation of the excitation functions in Fig. 6. As discussed below, the structure in the barrier distributions reveals details of the nuclear structure of the interacting nuclei.

Before attempting to interpret the barrier distributions for each reaction, it is worthwhile establishing that the features of the distributions are insensitive to effects of the systematic uncertainties, referred to in Sec. III A, and insensitive to the various corrections made to the cross sections. This is done in Fig. 8 for reactions with the ^{144}Sm target, for which the

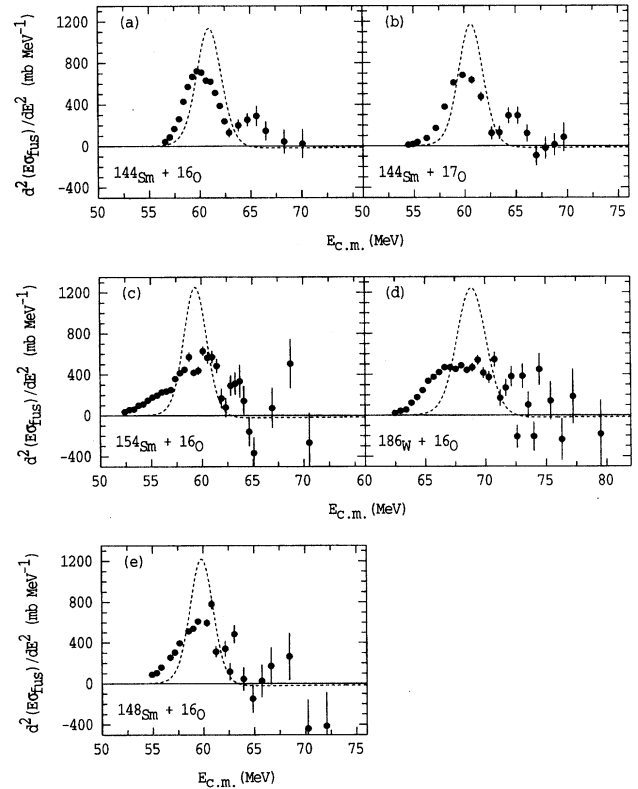


FIG. 7. Experimental barrier distributions for the indicated reactions. The dashed curves are extracted from the calculated excitation functions in Fig. 6 and hence show the single barrier which best reproduces the higher energy cross sections.

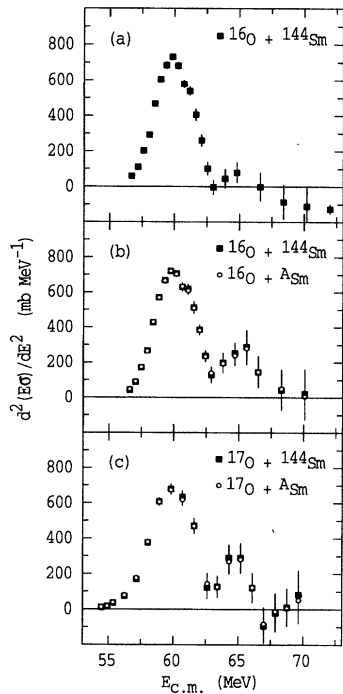


FIG. 8. Barrier distributions for the indicated reactions extracted (a) using cross sections assumed to be proportional to the measured differential cross sections at 2° , (b) and (c) from the total cross sections assuming the target to be 100% ^{144}Sm , open circles, and after correction for the contributions from the heavier Sm isotopes, filled squares.

largest corrections have been made. Whilst systematic errors may affect the cross sections they would need to have a strong energy dependence to significantly affect the *shape* of the extracted barrier distributions. For instance, the use of an incorrect detection efficiency simply results in a rescaling of the barrier distributions, without affecting the relative barrier weights. Systematic errors associated with the conversion of the measured differential values to total cross sections are expected to have the largest energy dependence. The effect of assuming that this conversion is independent of energy is shown in Figs. 8(a). Even with this extreme assumption, two peaks in the barrier distribution are still evident, although now the distribution becomes increasingly negative at the higher energies.

The effects on the barrier distributions of the corrections for the contamination of the ^{144}Sm target by heavier isotopes of samarium are shown in Figs. 8(b) and 8(c), for the ^{16}O and ^{17}O reactions, respectively. Each figure shows two overlapping barrier distributions derived from the use of the uncorrected cross sections, extracted assuming that the target was 100% ^{144}Sm (open circles) and from the cross sections after correction for the contributions of the heavier Sm isotopes (filled squares). At the lowest energy, half the cross section is estimated to result from the heavy impurities although the effects of the corrections reduce rapidly with energy and become only a fraction of one percent at energies above B_0 . Despite the large influence that the contaminants can have on the cross sections, the barrier distributions are affected only marginally, as seen in Fig. 8.

TABLE II. Fusion barriers and the diffuseness parameters of the nuclear potential obtained by fitting high energy fusion cross sections using a calculation with a single barrier. The values of B_0 and a are correlated; columns 3 and 5 indicate the ranges which increase the χ^2 values by 1. Higher values of B_0 correspond to lower values of a .

Reaction	B_0 (MeV)		a (fm)	
$^{144}\text{Sm} + ^{16}\text{O}$	61.10	0.05	0.84	0.03
$^{144}\text{Sm} + ^{17}\text{O}$	60.68	0.07	0.92	0.04
$^{148}\text{Sm} + ^{16}\text{O}$	59.85	0.08	1.05	0.04
$^{154}\text{Sm} + ^{16}\text{O}$	59.40	0.05	1.10	0.04
$^{186}\text{W} + ^{16}\text{O}$	68.90	0.06	1.11	0.04

It is therefore clear that the features in the barrier distributions are real and are not artifacts of the data reduction techniques.

IV. ANALYSIS AND DISCUSSION

The cross sections for each reaction have been fitted with a barrier penetration model, at energies above the barrier region, initially using only a single barrier. For these reactions this corresponds to fitting cross sections greater than 200 mb. The calculated cross sections at these energies are very sensitive to the average barrier height but are relatively insensitive to the form or magnitude of the coupling. Thus the parameters defining the nuclear potential between the interacting nuclei, in the absence of channel coupling, can be obtained. The nuclear potential was assumed to have an exponential form in the region of the barrier and it can then be conveniently parameterized in terms of the barrier height B_0 for the $l = 0$ partial waves and the diffuseness a of the potential. These parameters are presented in Table II and the associated excitation functions are shown by the dotted lines in Fig. 6.

A striking feature of the nuclear potentials in Table II is the consistently large values of the diffuseness parameters compared with the *average* value of 0.63 fm [29] extracted from elastic scattering data, especially for the reactions with the deformed targets. These values for the ^{154}Sm and ^{186}W reactions are slightly lower than those previously published [19,21] due to the omission of the highest energy points from the present analysis. These points were rejected because of uncertainties in the elastic scattering cross sections in the monitor detectors, at 30° ; the elastic scattering may not be Rutherford at beam energies as high as 110 MeV. The χ^2_ν for both reactions, in fitting the cross sections above 200 mb, decreased by a factor of 3 when one or two of the highest energy points were excluded from the fit. This change in a also results in changes in the extracted deformation parameters for these reactions, as shown below. Large values of the diffuseness from fusion analyses are not restricted to our measurements or to this mass region. For example, in Ref. [30], a value of $a = 0.75$ fm was required to fit the measured fusion data for $^{144}\text{Sm} + ^{16}\text{O}$ although a value of only 0.3 fm gave the best fit to elastic scattering data. Also, a value of 1.2 fm is obtained [31] for analysis of fusion for $^{40}\text{Ca} + ^{40}\text{Ca}$ [32] and some theoretical support for a large diffuseness comes from a double folding potential [33].

The difference in the a values consistently obtained in the analysis of fusion and elastic scattering data may arise, at least in part, from their different treatment of the high l grazing collisions associated with transfer reactions. The fusion model must scatter such partial waves to prevent them from contributing to the fusion cross section and this requires a high barrier for these l waves. In contrast, the scattering calculations must allow these high l waves to pass over the barrier and to be absorbed, to prevent them from appearing in the elastic channel. This requires lower barriers for high l -values. The diffuseness parameter determines how the barrier heights vary with angular momentum and a larger value of a gives barriers which increase more rapidly with l , giving qualitative support to the above arguments.

The inconsistency in the a values extracted from scattering and fusion data demonstrates the problems inherent in considering specific channels in isolation. The potentials extracted from such analyses are presumably “effective” ones, appropriate for describing that particular channel only; they should not be regarded as representing the true potentials. Only when all the relevant channels are considered simultaneously, in a full coupled-channels calculation, is it likely that the interaction potential can be extracted.

Although the interesting features of an excitation function, those which reflect the role of nuclear structure, are displayed at energies around the average barrier, precise measurements at higher energies are very important in the detailed analysis and interpretation. These data place strict limits on the effective nuclear potential parameters. Without such restrictions it may be possible to vary barrier height or diffuseness parameters to improve the fit to low energy cross sections. Even small changes in these nuclear parameters change the calculated low energy cross sections dramatically, even in the absence of coupling. It should be noted that there is some sensitivity of the calculated high energy cross sections to the coupling. For all reactions, the *average* barrier energy had to be adjusted slightly, compared with the single barrier in Table II, in order to retain the fit to these data when coupling effects were included. Increases of ≤ 0.3 MeV were required but the diffuseness parameters were unchanged.

A. The $^{144}\text{Sm} + ^{16}\text{O}$, ^{17}O reactions

For these reactions, the coupling scheme is expected to be relatively simple because the degree of collectivity associated with the semimagic nucleus ^{144}Sm is small. Indeed, a previous fusion analysis has treated ^{144}Sm as inert [23]. The excitation functions are shown in Figs. 6(a) and 6(b) and the barrier distributions in Figs. 7(a) and 7(b). Calculations assuming no coupling are shown by the dashed lines in these figures; clearly they are inconsistent with experiment. The experimental barrier distributions for both reactions are dominated by barrier strength around 60 MeV, whose width is close to that of the single barrier. Both show additional strength near 65 MeV and it appears that a second barrier exists which is almost completely resolved from the main one. Since the two reactions have significantly different Q values for one- and two-particle transfer reactions and the projectiles have different structure, the consistency of this feature strongly implies that it is associated with inelastic excitation of ^{144}Sm .

We have performed a series of calculations to investigate the structure in the experimental barrier distributions. The simplified coupled-channels code CCMOD [34] has been used to determine the effects of coupling to inelastic channels [22]. The code is a version of CCDEF [35] which has been modified to perform the matrix diagonalization exactly at each value of the internuclear separation r .

Inelastic coupling strengths were included using

$$F_{\text{inel}}(r) = \frac{\beta_\lambda}{\sqrt{4\pi}} \left[-R \frac{dV_n(r)}{dr} + \frac{3Z_1 Z_2 e^2}{(2\lambda + 1)} \frac{R^\lambda}{r^{\lambda+1}} \right], \quad (5)$$

where β_λ is the deformation parameter associated with multipolarity λ , R is the radius of the nucleus which is excited, taken to be $1.06A^{1/3}$ fm, and $V_n(r)$ is the nuclear potential. The β_λ were obtained from measured transition probabilities [36] using

$$\beta_\lambda = \frac{4\pi}{3ZR^\lambda} \left[\frac{B(E\lambda)\uparrow}{e^2} \right]^{1/2}. \quad (6)$$

Having adjusted the nuclear potential parameters to fit the high energy data, and in view of the approximations inherent in the simplified coupled-channels code, no further parameter adjustments have been made. The most important channels associated with excitation of ^{144}Sm are expected to involve those states with the largest $B(E\lambda)\uparrow$ values, i.e., the first 2^+ and 3^- states. The associated deformation parameters, from Eq. (6), are $\beta_2 = 0.11$ and $\beta_3 = 0.21$. Since an effective deformation [37] may be estimated by combining these in quadrature, the larger value of the latter suggests the coupling to the inelastic 3^- channel should be dominant. Considering first the ^{16}O reaction, including the 3^- state in the calculation gives a good representation of the data, as shown in Figs. 9(a) and 9(b). The quality of the representation is modified only marginally by the addition of the 2^+ state in the calculation, also shown in Figs. 9(a) and 9(b), and this confirms that the effects of target octupole excitation are dominant in this case.

Frequently the effects of inelastic excitation of the projectile are included in these CCMOD calculations. However, inclusion of the inelastic channel associated with the excitation of the most collective state in ^{16}O , the 3^- state at 6.1 MeV with $\beta_3 = 0.71$, destroys the agreement between experiment and theory as shown in Figs. 9(c) and 9(d). The coupling pushes barrier strength above 70 MeV and depletes strength around 65 MeV, giving a barrier distribution which is inconsistent with the measured one. This demonstrates that it is inappropriate to include the excitation of ^{16}O in simple coupled-channels calculations, which do not account for dynamical effects of the coupling, and supports the conclusions of Ref. [38] that the role of projectile excitation, specifically in the $^{148}\text{Sm} + ^{16}\text{O}$ reaction, would be strongly suppressed because of “proximity” and dynamical effects. We have performed a series of CCMOD calculations with reduced strength for the ^{16}O coupling. The data suggest that the coupling strength associated with excitation of ^{16}O must be reduced by at least a factor of 4 compared with that calculated using Eq. (5).

It is instructive to note that the increase in low energy cross sections resulting from the coupling to the ^{16}O excita-

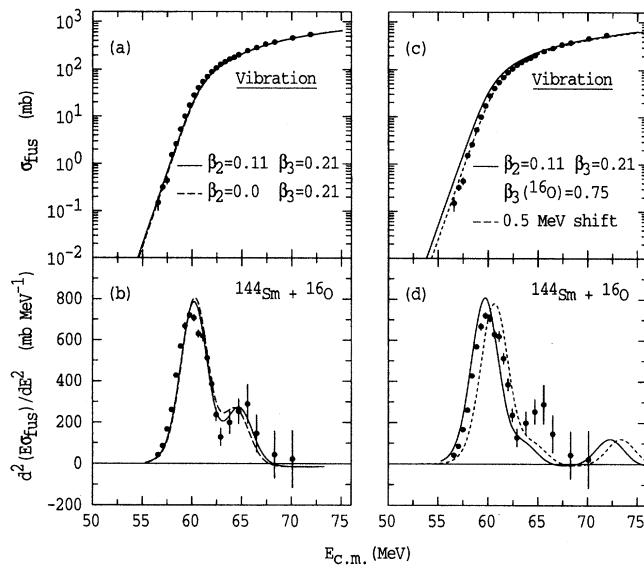


FIG. 9. Comparison of the measured excitation function and extracted barrier distribution for $^{144}\text{Sm} + ^{16}\text{O}$ with various calculations. The solid lines in (a) and (b) are the results of coupling to inelastic channels involving excitation of the 2^+ and 3^- states of ^{144}Sm ; the dashed lines show the effect of omitting the 2^+ state. The solid lines in (c) and (d) are the results of including the excitation of the 3^- state of the projectile. The dashed lines are the same calculation with the average barrier increased by 0.5 MeV in order to fit the low energy cross sections.

tion can be largely compensated by an increase in the height of the average barrier by 0.5 MeV, as shown in Fig. 9(c). Indeed, over the energy range displayed this excitation function appears to reproduce the data at least as well as the calculation in Fig. 9(a). However, the barrier distribution in Fig. 9(d) is still poorly reproduced and calculated cross sections at the highest energies are now a few percent too low. This comparison serves to reinforce several important points. Simply adjusting the parameters of a calculation to give what appears to be a fit to the low energy cross sections, as done in Ref. [39] for instance, does not ensure that the correct couplings have been included. Accurate data at high energies are essential to constrain the height of the average barrier. The barrier distribution representation offers a much more sensitive method of determining the important couplings. This latter point is particularly important in a case such as this because the calculated excitation function is not an ideal representation of the data and the χ^2_ν is much greater than unity. A statistical analysis of a fit to the data may not distinguish between different models which have similarly large χ^2_ν values but the major contributions to χ^2_ν may come from different energy regions where the fits are systematically poor. Such a region can be seen in Fig. 9(a) where the data are consistently higher than the calculation around 60 MeV. Under these circumstances, a calculation which has the *qualitative* features displayed in the experimental barrier distribution, like that in Fig. 9(b), is much more likely to contain the appropriate channel couplings than one which does not, as in Fig. 9(d).

In considering the reaction with the ^{17}O projectile, its

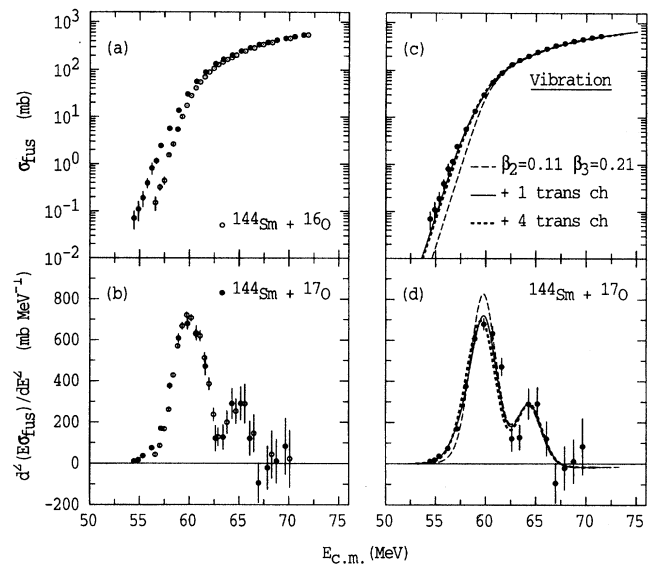


FIG. 10. Comparison of (a) the measured excitation functions and (b) extracted barrier distributions for $^{144}\text{Sm} + ^{16}\text{O}$ and for $^{144}\text{Sm} + ^{17}\text{O}$. The ^{17}O data are compared with calculations which involve excitation of 2^+ and 3^- states of ^{144}Sm (long dashed lines) in (c) and (d). The solid lines show the effects of a neutron transfer channel with positive Q -value of +2.6 MeV. The short dashed lines result from distributing the transfer strength over four channels.

inelastic excitation has not been included in the calculations since its collective properties may be expected to be similar to those of ^{16}O . The excitation functions for the ^{16}O and ^{17}O reactions are compared directly in Fig. 10(a). The cross sections are very similar at high energies and the barrier distributions, in Fig. 10(b), are also the same above the main peak. However, at low energies the cross sections for the ^{17}O reaction are more than four times higher than those for ^{16}O and the increased cross-section is reflected in the barrier distribution as a weak tail extending to low energies. A calculation using inelastic coupling to the 2^+ and 3^- states of ^{144}Sm , with strengths identical to those which described the ^{16}O data, fails to fit the ^{17}O data, as shown by the dashed lines in Figs. 10(c) and 10(d); clearly additional coupling is required for the heavier projectile. An increased cross-section will result from any form of extra coupling, as was shown in Fig. 2 and in the associated discussion; however, the type of coupling required is not immediately apparent in the excitation function. The *assumption* that transfer plays a role is not unreasonable because of the loosely bound neutron in ^{17}O . In contrast, no theoretical guidance is required to interpret the barrier distribution. In this reaction, barrier strength below the main one can *only* be produced by coupling to a channel with a *positive* Q value, which rules out inelastic channels. The additional channel must be associated with transfer. The reaction $^{144}\text{Sm}(^{17}\text{O}, ^{16}\text{O})^{145}\text{Sm}$ has a ground-state Q value of +2.6 MeV and is the obvious candidate for inclusion in the calculations.

The effects of transfer can be treated approximately in the code CCMOD which uses coupling of the form [9]

$$F_{\text{tran}}(r) = \frac{\mathcal{K}}{\sqrt{4\pi}} \exp\left[-\frac{r-R_b}{a}\right], \quad (7)$$

where R_b is the sum of the radii of the interacting nuclei and $a = 1.2$ fm. Coupling to the ground-state transfer channel has been included in a calculation where the strength \mathcal{K} of the coupling was adjusted to fit the data; none of the other parameters were adjusted. The calculated excitation function and barrier distribution, shown in Figs. 10(c) and 10(d), respectively, are in excellent agreement with the experimental data. The best fit was obtained with the value of $\mathcal{K} = 2.8$ MeV. This compares with an average value of ≈ 3 MeV for single nucleon transfer in a range of reactions [40], calculated using spectroscopic factors of unity, though these calculated values vary by almost two orders of magnitude, depending on the nucleon orbitals and transferred angular momentum.

It is interesting to note that the barrier strength below the main peak, introduced as a result of coupling to the transfer channel, is about a factor of 3 smaller than that above the main peak, which arises mainly from coupling to inelastic channels. The inelastic coupling strength is weak in this case, because of the low β_λ values of the semimagic ^{144}Sm . On the other hand, the single-neutron transfer to low lying states is associated with reasonably large spectroscopic factors [41] and is therefore expected to be a strong transfer channel. Thus it is not unreasonable to conclude that individual transfer channels will generally have a minor effect in redistributing barrier strength. Whilst the effects of a positive Q -value channel may be easily observed, the effects of a transfer channel with a negative Q value are likely to be difficult to identify when even the weakest inelastic channels are involved. This conclusion is supported by the results of Ref. [42] for the fusion of $^{58}\text{Ni} + ^{60}\text{Ni}$, where the coupling effects were dominated by multiphonon excitations and the anticipated two-neutron transfer channel could not be identified. However, transfer might be expected to have a significant effect when the number of transfer channels is large compared with the number of inelastic channels [9].

The initial assumption that transfer to the ground state of ^{145}Sm is the only important channel is too simple since it is expected that several states in ^{145}Sm will be populated in the stripping reaction. In the $^{144}\text{Sm}(^{13}\text{C}, ^{12}\text{C})^{145}\text{Sm}$ reaction, transfer to four single-particle states, $2f_{7/2}$, $3p_{3/2}$, $3p_{1/2}$, and $2f_{5/2}$, was observed [41]. The transfer strength to each single-particle state was similar but was distributed over several energy levels, with centroid energies of 0.0, 1.43, 1.61, and 1.78 MeV, respectively [41]. We have therefore included four transfer channels in a second CCMOD calculation. A common coupling strength was used for all channels and it was adjusted to give a reasonable representation of the data, as shown in Figs. 10(c) and 10(d). A fit to the data of similar quality to that for the one transfer channel was obtained using $\mathcal{K} = 1.4$ MeV. Now the coupling to each individual channel is reduced although the total effective coupling strength is unchanged since the individual strengths are added in quadrature. Thus our measurement gives an estimate of the total coupling strength but gives no indication of its distribution between the available transfer channels. It would be necessary to use a reaction with an isolated positive Q -value channel in order to determine its individual coupling strength.

The excellent representation of the data for both the ^{16}O and ^{17}O reactions could be to some extent fortuitous. As

discussed earlier, the nuclear potential is an effective one which requires a large diffuseness to fit high energy cross sections. It is not obvious that this is the appropriate potential to use in Eq. (5). Also the coupling strengths depend on the choice of the nuclear radius parameter used in Eqs. (5) and (6). The original choice of 1.06 fm was somewhat arbitrary and was used in calculations for $^{154}\text{Sm} + ^{16}\text{O}$ [19]. For consistency, the coupling strengths for all the reactions discussed here are evaluated using a radius parameter of 1.06 fm and using the effective nuclear potential which fits the high energy data. Because of these uncertainties, as well as approximations implicit in the CCMOD calculations, no attempt has been made to obtain the optimum fit to these cross sections by adjusting any parameters. For the same reasons care should also be taken in drawing conclusions from the β_λ values which provide good representations of the data.

Despite these limitations, the clear qualitative agreement between the calculated and experimental barrier distributions strongly supports the above assignments and unambiguously demonstrates the effects on fusion of channels associated with inelastic excitation of the target nucleus and single neutron transfer. Our data also indicate that projectile excitation appears to play an insignificant role in these reactions.

B. The ^{154}Sm , $^{186}\text{W} + ^{16}\text{O}$ reactions

The measured excitation functions [16,21] are shown in Figs. 6(c) and 6(d), respectively. The dashed curves are the results of calculations using single barriers resulting from the nuclear potentials in Table II. The barrier distributions extracted from these data are shown in Figs. 7(c) and 7(d). They are compared with the distributions calculated for the average barrier of each reaction. The obvious features are that the experimental distributions are very wide relative to the single barrier and extend to lower energies compared with the ^{144}Sm distributions. This is not surprising since the target nuclei are known to have permanent quadrupole deformations and a wide range of barriers would be expected classically, due to the random orientations of the deformed target nuclei.

The fusion excitation functions have been calculated using Hill-Wheeler transmission coefficients associated with a set of fusion barriers which depend on the angle θ between the symmetry axis of the deformed target nucleus and the beam direction. The projectile is treated as inert. The barriers depend on l and they are calculated from the maximum in the potential

$$V(r, \theta, l) = V_C(r, \theta) + V_N(r, \theta) + V_l(r), \quad (8)$$

where $V_C(r, \theta)$ is the Coulomb potential including quadrupole and hexadecapole terms, expanded to order β_2^2 and β_4 , and $V_l(r)$ is the usual centrifugal potential. The nuclear potential $V_N(r, \theta)$ uses parameters which fit the high energy data but its exponent contains a factor $R(\theta)/a$ with $R(\theta) = R_T[1 + \beta_2 Y_2(\theta) + \beta_4 Y_4(\theta)]$ to account for the dependence of the radius of the deformed target nucleus on its orientation. R_T is the mean radius of the target nucleus given by $1.06A^{1/3}$ fm. The barrier heights $B(l, \theta)$ were calculated numerically for each l value and target nucleus orientation. The fusion cross sections were then evaluated using

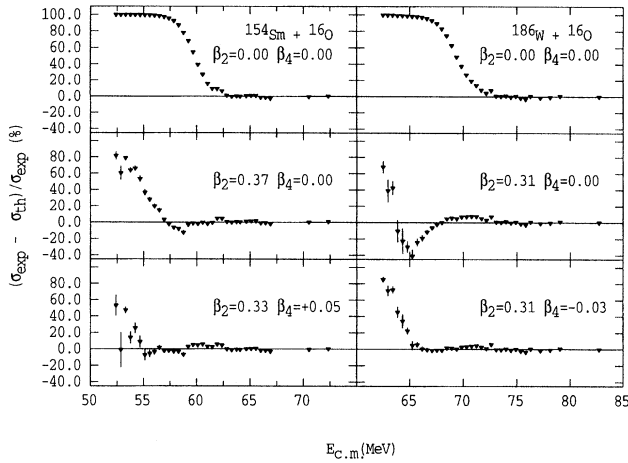


FIG. 11. Percentage deviation of the calculated cross sections from those measured for the $^{154}\text{Sm} + ^{16}\text{O}$ and $^{186}\text{W} + ^{16}\text{O}$ reactions for various combinations of β_2 and β_4 . The optimum fits in the lower panels underestimate the data at the lower energies for both reactions.

$$\sigma_{\text{fus}} = \sum_l \int_0^{\pi/2} \sigma_{\text{fus}}(l, \theta) d\theta, \quad (9)$$

where

$$\sigma_{\text{fus}}(l, \theta) = \frac{\pi \chi^2(2l+1)}{1 + \exp\left[\frac{2\pi(B(l, \theta) - E)}{\hbar \omega(l, \theta)}\right]}. \quad (10)$$

In practice, the integration in Eq. (9) was performed using an eigenchannel formalism [43] using 20 channels which represent different orientations of the classical shape with geometric weights associated with the probability of encountering the nucleus with that orientation. Alternatively, the 20 channels can be considered as representing members of the ground state rotational band of a deformed nucleus.

Early attempts to fit fusion data, using a distribution of barriers associated with a static deformation [3,23,28], yielded very low values of β_2 . Reasons for this have been discussed elsewhere [19]. For comparison with those previous results, and because the model approximations are less severe for deformed nuclei, we chose to fit the data by adjusting the deformation parameters. Initially, the β_2 deformation parameters for ^{154}Sm and ^{186}W were adjusted to give the best fits to the excitation functions, defined as those giving the minimum χ^2_ν value. These fits give reasonable descriptions of the data, supporting the expectation that the fusion enhancement is largely due to the target deformation. The results are presented in Fig. 11 as differences of the experiment and theory as a percentage of the experimental cross section. The top panels in Fig. 11 show the deviations obtained from a calculation using the single barrier in Table II.

The inclusion of a β_2 deformation dramatically improves the agreement, as seen in the center panels of Fig. 11, giving values of χ^2_ν of 17 for each reaction compared with ≈ 800 when using the single barrier. The corresponding excitation

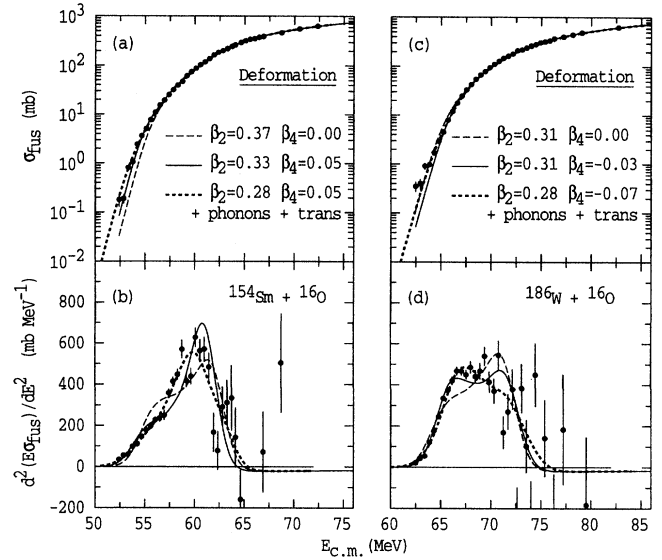


FIG. 12. Comparison of the measured excitation functions and barrier distributions for $^{154}\text{Sm} + ^{16}\text{O}$ and $^{186}\text{W} + ^{16}\text{O}$ with calculations assuming each has a static deformation. The long dashed lines are optimum fits assuming quadrupole deformations, the solid curves include hexadecapole deformations (see Fig. 11 also). The short dashed lines show the effects of additional coupling to octupole and quadrupole vibrations and a positive Q value transfer channel. The sensitivity of the extracted deformation parameters to these couplings can be seen.

functions and barrier distributions are presented in Fig. 12. The best fits to the excitation functions are achieved with β_2 values of 0.37 and 0.31 for ^{154}Sm and ^{186}W , respectively. The fits to the cross sections are still poor at low energies, although the agreement now extends to lower energies relative to the single barrier calculations. Also the calculated barrier distributions, shown in Fig. 12, show clear systematic deviations from the data and the β_2 values are larger than the accepted values of ≈ 0.30 and ≈ 0.24 from Coulomb excitation studies [44,45]. These failures suggest the data are sensitive to nuclear properties other than the quadrupole deformation.

The ^{154}Sm and ^{186}W nuclei are known to have significant hexadecapole deformations and the results of including such a term in the calculations are shown in Figs. 11 and 12. The ranges over which the fits are good now extend to lower energies, as seen in the lower panels of Fig. 11, and the overall fits to the excitation functions are improved, χ^2_ν now being 7 for ^{154}Sm and 6 for ^{186}W . However, at the lowest energies the cross sections in the ^{186}W reaction are fitted less well, as seen in Figs. 11 and 12(c), whereas the fit in the ^{154}Sm case is improved, Fig. 12(a). There is good qualitative agreement in the shapes of the barrier distributions in Figs. 12(b) and 12(d). The optimum fits to the cross sections are obtained with deformation parameters $\beta_2 = 0.33$ and $\beta_4 = 0.05$ for ^{154}Sm and $\beta_2 = 0.31$ and $\beta_4 = -0.03$ for ^{186}W . The β_2 parameters are slightly larger than those in Refs. [19,21] as a result of using a smaller diffuseness parameter in the nuclear potential. Again this illustrates the need for good quality data at energies above the barrier as

well as indicating the sensitivity of the extracted deformation parameters to the nuclear potential.

The largest differences between the deformation parameters extracted from fusion and those from Coulomb excitation and inelastic α -scattering measurements [45] occur for ^{186}W , where the nonfusion values are $\beta_2 = 0.24$ and $\beta_4 = -0.08$. It was demonstrated in Ref. [21] that smaller deformation parameters were required to fit the fusion data when additional couplings to vibrational states in the target were included in the calculations. The need for additional coupling for both reactions is suggested by the failure of the calculations to reproduce the lowest energy data using only deformations. It is also clear in the ^{186}W case that the height of the plateau in the barrier distribution in Fig. 12(d), in the energy range 66 MeV to 69 MeV, is underestimated by the theory. This latter feature could be reproduced in the calculation using a smaller β_2 value, a more negative β_4 value, or a combination of both. The resultant decrease in the width of the barrier distribution, and in the cross sections at low energies, cannot then be compensated by including couplings to the known vibrational 2^+ and 3^- states in ^{186}W . However, the proton stripping channel has an *effective* positive Q value of +2 MeV, given by the difference between the ground state transfer Q value and the optimum Q value when changes in Coulomb energy are taken into account. Since a positive- Q transfer channel has been shown to play an important role in the $^{144}\text{Sm} + ^{17}\text{O}$ reaction, it has also been included in a CCMOD calculation in addition to the phonon couplings used in Ref. [21]. The coupling strengths for the inelastic channels (two 2^+ states and one 3^- state) were evaluated from published $B(E\lambda)\uparrow$ values [46] using Eq. (5) whilst that for the transfer channel was taken to be 2.8 MeV, the value extracted from the ^{144}Sm data. The optimum fit to the data, obtained by adjusting the static deformation parameters, is shown in Figs. 12(c) and 12(d) and the data are reproduced surprisingly well in all respects, using $\beta_2 = 0.28$ and $\beta_4 = -0.07$. Both these values are closer to those obtained from inelastic scattering studies; now the fit to the cross sections has $\chi^2_\nu = 3$.

Since ^{154}Sm has vibrational states [47] equivalent to those in ^{186}W and the reaction also has a similar positive Q value (+1.5 MeV) transfer channel, the ^{154}Sm cross-sections have been calculated as described above. The results are displayed in Figs. 12(a) and 12(b). Again the fit is remarkably good, giving $\chi^2_\nu = 4$ using $\beta_2 = 0.28$ and $\beta_4 = 0.05$.

It is not clear to what degree these last calculations are parameter fitting. However, they do serve to demonstrate the sensitivity of the excitation functions and barrier distributions to relatively weak coupling even in the presence of the strong effects expected from static deformations. They also illustrate the dependence of the extracted deformation parameters on these additional couplings.

Despite these uncertainties, it is clear from the qualitatively different shapes of the experimental barrier distributions for the two reactions, as illustrated in Fig. 12, that the fusion excitation functions are very sensitive to both quadrupole and hexadecapole deformations. Fusion data may thus be used to estimate the magnitude of deformation parameters and importantly to determine their signs, removing ambiguities often associated with other techniques.

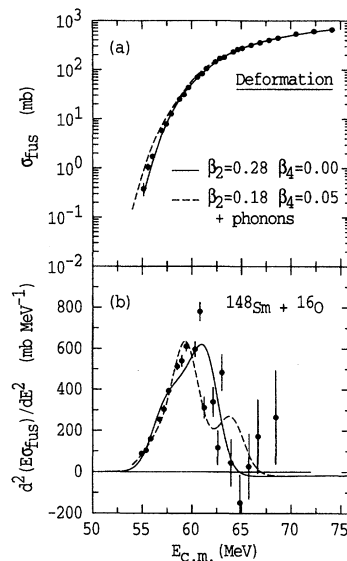


FIG. 13. Fits to the excitation function and barrier distribution assuming ^{148}Sm has a static deformation. The dashed lines result from a smaller, more reasonable, deformation with additional coupling to channels involving vibrational excitations.

C. The $^{148}\text{Sm} + ^{16}\text{O}$ reaction

Theoretically, the form required for the couplings in this vibrational nucleus is not as clear as those for the near-spherical and deformed coupling cases discussed above. The excitation function is shown in Fig. 6(e) and the barrier distribution in Fig. 7(e). The distribution is much wider than that for the single barrier required to fit the high energy data and it appears to have an asymmetry similar to, but smaller than, that for ^{154}Sm . This form of asymmetry, with a tail extending to low energies, is characteristic of a static positive β_2 . Positive Q -value transfer reactions can also produce barrier strength at low energies but there are no such single-particle transfer channels for this reaction. The data have therefore been analyzed using the same procedure as that for the deformed nuclei in the preceding section. The optimum fit to the excitation function gives a χ^2_ν of ≈ 7 and is obtained with $\beta_2 = 0.28$ and $\beta_4 = 0.0$. The excitation functions and barrier distributions are displayed in Fig. 13.

The value of β_2 is high, 50% larger than the value of 0.18, extracted from the $B(E2)\uparrow$ using Eq. (5). The possible effects of additional couplings have been investigated by including known 2^+ and 3^- states of ^{148}Sm in a CCMOD calculation, again using established $B(E\lambda)\uparrow$ values [48]. The results of the calculation using static deformation parameters of $\beta_2 = 0.18$ and $\beta_4 = 0.05$ are shown in Fig. 13. The cross sections are well reproduced and the barrier distribution gives an improved fit to the data in the range below the peak. The additional coupling produces structure in the barrier distribution at higher energies where our data show a significant degree of scatter. The effects of other couplings, to transfer channels with negative Q values for instance, might tend to wash out this calculated feature; more precise measurements would be required to confirm its presence, or absence.

The overall width of the barrier distribution suggests that coupling between successive members of a collective band is important in this reaction. It does appear that a good representation of the data can be achieved using accepted deformation parameters in our calculations, provided the expected weak couplings are also included. This does not necessarily mean that the use of a static deformation is correct. It is also possible that the more realistic option of coupling between several members of a vibrational band can produce similar features, although a calculation [49] in which the vibrational nature of ^{148}Sm was reproduced using an interacting boson model, gave a near symmetric barrier distribution.

V. CONCLUSION

There had been a general acceptance of the notion that fusion excitation functions are smooth and featureless. This attitude had arisen mainly because cross sections were typically measured with relatively poor precision and at only a small number of energies. Under these circumstances, a range of models with different parameters could fit the data equally well, giving the impression that fusion excitation functions did not serve as a good test of models.

We have measured five fusion excitation functions with small, well-defined energy intervals and with sufficiently high precision to demonstrate that these excitation functions contain structure which depends in detail on the properties of the interacting nuclei. This structure is most dramatically seen when $d^2(E\sigma_{\text{fus}})/dE^2$ is plotted as a function of energy. This form of presentation is very useful in that it accentuates the unique features of each excitation function. Comparison

of our data with model calculations demonstrates that the interpretation of $d^2(E\sigma_{\text{fus}})/dE^2$ as a distribution of fusion barriers is justified. This "snap-shot" of the important barriers involved in a fusion reaction then makes interpretation of the sub-barrier fusion process much clearer.

The barrier distributions for the reactions with the semimagic ^{144}Sm nucleus show structures which can readily be associated with specific inelastic and transfer channels. Importantly, the barrier distribution can indicate which channels are *not* playing a significant role in fusion; the inclusion in the simplified coupled-channels codes of states in projectiles such as ^{16}O is not warranted.

In the reactions involving the deformed target nuclei, the barrier distributions are dominated by deformation effects. In particular, the role of the hexadecapole deformation is immediately evident in the qualitative differences between the two barrier distributions. At present, the fusion method cannot be regarded as a precise way of determining the magnitudes of deformation parameters although it does have the important benefit of giving their signs without ambiguity. Although the deformation effects are strong, the excitation functions show that additional relatively weak channels are important. Thus fusion may prove to be a most sensitive probe of channel coupling.

Fusion excitation functions can now be measured with high precision. However, comparison of such data with the results of the fusion models in common use may be limited because of the approximations made in these models. The refinement of the models to achieve a degree of precision and reliability comparable to the data presents an interesting challenge to theory.

-
- [1] C.Y. Wong, *Phys. Rev. Lett.* **31**, 766 (1973).
 - [2] L.C. Vaz and J.M. Alexander, *Phys. Rev. C* **10**, 464 (1974).
 - [3] R.G. Stokstad, Y. Eisen, S. Kaplanis, D. Pelte, U. Smilansky, and I. Tserruya, *Phys. Rev. Lett.* **41**, 465 (1978); *Phys. Rev. C* **21**, 2427 (1980).
 - [4] W. Reisdorf, F.P. Hessberger, K.D. Hildenbrand, S. Hofmann, G. Münzenberg, K.-H. Schmidt, J.H.R. Schneider, W.F.W. Schneider, K. Sümmerer, G. Wirth, J.V. Kratz, and K. Schlitt, *Phys. Rev. Lett.* **49**, 1811 (1982); *Nucl. Phys.* **A438**, 212 (1985).
 - [5] H. Esbensen, *Nucl. Phys.* **A352**, 147 (1981).
 - [6] M. Beckerman, M. Salomaa, A. Sperduto, H. Enge, J. Ball, A. DiRienzo, S. Gazes, Yan Chen, J.D. Molitoris, and Mao Naifeng, *Phys. Rev. Lett.* **45**, 1472 (1980).
 - [7] U. Jahnke, H.H. Rossner, D. Hilscher, and E. Holub, *Phys. Rev. Lett.* **48**, 17 (1982).
 - [8] C.H. Dasso, S. Landowne, and A. Winther, *Nucl. Phys.* **A405**, 381 (1982); **A407**, 221 (1983).
 - [9] R.A. Broglia, C.H. Dasso, S. Landowne, and G. Pollarolo, *Phys. Lett.* **133B**, 34 (1983).
 - [10] R.A. Broglia, C.H. Dasso, and S. Landowne, *Phys. Rev. C* **32**, 1426 (1985).
 - [11] M.A. Nagarajan, A.B. Balantekin, and N. Takigawa, *Phys. Rev. C* **34**, 894 (1986).
 - [12] H.J. Krappe, K. Mohring, M.C. Nemes, and H. Rossner, *Z. Phys. A* **314**, 23 (1983).
 - [13] P.H. Stelson, H.J. Kim, M. Beckerman, D. Shapira, and R.L. Robinson, *Phys. Rev. C* **41**, 1584 (1990).
 - [14] J.G. Keller, K.-H. Schmidt, F.P. Hessberger, G. Münzenberg, and W. Reisdorf, *Nucl. Phys.* **A452**, 173 (1986).
 - [15] N. Rowley, G.R. Satchler, and P.H. Stelson, *Phys. Lett. B* **254**, 25 (1991).
 - [16] J.X. Wei, J.R. Leigh, D.J. Hinde, J.O. Newton, R.C. Lemmon, S. Elfström, J.X. Chen, and N. Rowley, *Phys. Rev. Lett.* **67**, 3368 (1991).
 - [17] G. Duchêne, P. Romain, F.A. Beck, Ph. Benet, D. Disdier, B. Haas, B. Lott, V. Rauch, F. Scheibling, J.P. Vivien, S.K. Basu, E. Bozek, and K. Zuber, *Phys. Rev. C* **47**, 2043 (1993).
 - [18] M.L. Halbert, J.R. Beene, D.C. Hensley, K. Honkanen, T.M. Semkow, V. Abenante, D.G. Sarantites, and Z. Li, *Phys. Rev. C* **40**, 2558 (1989).
 - [19] J.R. Leigh, N. Rowley, R.C. Lemmon, D.J. Hinde, J.O. Newton, J.X. Wei, J.C. Mein, C.R. Morton, S. Kuyucak, and A.T. Kruppa, *Phys. Rev. C* **47**, R437 (1993).
 - [20] J.R. Leigh, M. Dasgupta, C.R. Morton, D.J. Hinde, R.C. Lemmon, J.O. Newton, and J.X. Wei, in *Proceedings of the International Workshop on Heavy-ion Reactions with Neutron-rich Beams*, RIKEN, Saitama, Japan 1993, edited by M. Ishihara, N. Takigawa, and S. Yamaji (World Scientific, Singapore, 1993), p. 29.
 - [21] R.C. Lemmon, J.R. Leigh, J.X. Wei, C.R. Morton, D.J. Hinde,

- J.O. Newton, J.C. Mein, and M. Dasgupta, *Phys. Lett. B* **316**, 32 (1993).
- [22] C.R. Morton, M. Dasgupta, D.J. Hinde, J.R. Leigh, R.C. Lemmon, J.P. Lestone, J.C. Mein, J.O. Newton, H. Timmers, N. Rowley, and A.T. Kruppa, *Phys. Rev. Lett.* **72**, 4074 (1994).
- [23] D.E. DiGregorio, J.O. Fernández Niello, A.J. Pacheco, D. Abriola, S. Gil, A.O. Macchiavelli, J.E. Testoni, P.R. Pascholati, V.R. Vanin, R. Liguori Neto, N. Carlin Filho, M.M. Coimbra, P.R. Silveira Gomes, and R.G. Stokstad, *Phys. Lett. B* **176**, 322 (1986).
- [24] J.X. Wei, J.R. Leigh, D.C. Weissner, J.O. Newton, S. Elfström, J.P. Lestone, J.X. Chen, D.G. Popescu, and D.J. Hinde, *Nucl. Instrum. Methods Phys. Res. A* **306**, 557 (1991).
- [25] R.H. Spear, D. C. Kean, M. T. Esat, A. N. R. Joye, and M. P. Fewell, *Nucl. Instrum. Methods* **147**, 455 (1977).
- [26] A. Gavron, *Phys. Rev. C* **21**, 230 (1980).
- [27] C.E. Beamis, T.C. Awes, J.R. Beene, R.L. Ferguson, H.J. Kim, F.K. McGowan, F.E. Obenshain, F. PLasil, P. Jacobs, Z. Frankel, U. Smilanski, and I. Tserruya, ORNL Physics Division Progress Report No. 6326, p. 110, 1980 (unpublished).
- [28] D.E. DiGregorio, M. di Tada, D. Abriola, M. Elgue, A. Etchegoyen, M.C. Etchegoyen, J.O. Fernández Niello, A.M.J. Ferrero, S. Gil, A.O. Macchiavelli, A.J. Pacheco, J.E. Testoni, P.R. Silveira Gomes, V.R. Vanin, R. Liguori Neto, E. Crema, and R.G. Stokstad, *Phys. Rev. C* **39**, 516 (1989).
- [29] P.R. Christensen and A. Winther, *Phys. Lett.* **65B**, 19 (1976).
- [30] D. Abriola, D.E. DiGregorio, J.E. Testoni, A. Etchegoyen, M.C. Etchegoyen, J.O. Fernández Niello, A.M.J. Ferrero, S. Gil, A.O. Macchiavelli, A.J. Pacheco, and J. Kittl, *Phys. Rev. C* **39**, 546 (1989).
- [31] N. Rowley, Nuclear Physics Appendix to the Daresbury Annual Report 1993 (unpublished).
- [32] H.A. Aljuwair, R.J. Ledoux, M. Beckerman, S.B. Gazes, J. Wiggins, E.R. Cosman, R.R. Betts, S. Saini, and O. Hansen, *Phys. Rev. C* **30**, 1223 (1984).
- [33] G.R. Satchler and W.G. Love, *Phys. Rep.* **55**, 183 (1979).
- [34] M. Dasgupta, A. Navin, Y.K. Agarwal, C.V.K. Baba, H.C. Jain, M.L. Jhingan, and A. Roy, *Nucl. Phys.* **A539**, 351 (1992).
- [35] C.H. Dasso and S. Landowne, *Comp. Phys. Commun.* **46**, 187 (1987); J.O. Fernández Niello, C.H. Dasso, and S. Landowne, *ibid.* **54**, 409 (1989).
- [36] J.K. Tuli, *Nucl. Data Sheets* **56**, 607 (1989).
- [37] A.T. Kruppa, P. Romain, M.A. Nagarajan, and N. Rowley, *Nucl. Phys.* **A560**, 845 (1993).
- [38] H. Esbensen, Jian-qun Wu, and G.F. Bertsch, *Nucl. Phys.* **A411**, 275 (1983).
- [39] P.R.S. Gomes, I.C. Charret, R. Wanis, G.M. Sigaud, V.R. Vanin, R. Liguori Neto, D. Abriola, O.A. Capurro, D.E. DiGregorio, M. di Tada, G. Duchêne, M. Elgue, A. Etchegoyen, J.O. Fernández Niello, A.M.J. Ferrero, S. Gil, A.O. Macchiavelli, A.J. Pacheco, and J.E. Testoni, *Phys. Rev. C* **49**, 245 (1994).
- [40] G. Pollarolo, R.A. Broglia, and A. Winther, *Nucl. Phys.* **A406**, 369 (1983).
- [41] S.T. Thornton, J.L.C. Ford, Jr., E. Friedland, C.A. Wiedner, and M. Goldschmidt, *Phys. Rev. C* **12**, 877 (1975).
- [42] A.M. Stefanini, D. Ackermann, L. Corradi, D.R. Napoli, C. Petrache, P. Spolaore, P. Bednarczyk, H.Q. Zhang, S. Beghini, G. Montagnoli, L. Mueller, F. Scarlassara, G.F. Segato, F. Soramel, and N. Rowley, *Phys. Rev. Lett.* **74**, 864 (1995).
- [43] R. Lindsay and N. Rowley, *J. Phys. G* **10**, 805 (1984).
- [44] H. Fischer, D. Kamke, H.J. Kittling, E. Kuhlman, H. Plicht, and R. Schormann, *Phys. Rev. C* **15**, 921 (1977).
- [45] I.Y. Lee, J.X. Saladin, J. Holden, J. O'Brien, C. Baktash, C. Beamis, Jr., P.H. Stelson, F.K. McGowan, W.T. Milner, J.L.C. Ford, Jr., R.L. Robinson, and W. Tuttle, *Phys. Rev. C* **12**, 1483 (1975).
- [46] R.B. Firestone, *Nucl. Data Sheets* **55**, 583 (1988).
- [47] R.G. Helmer, *Nucl. Data Sheets* **52**, 1 (1987); **69**, 507 (1993).
- [48] L.K. Peker, *Nucl. Data Sheets* **59**, 393 (1990).
- [49] A.B. Balantekin, J.R. Bennett, and S. Kuyucak, *Phys. Rev. C* **49**, 1079 (1994).